Hunt–Crossley model based force control for minimally invasive obotic surgery

A. Pappalardo [a], A. Albakri [b], C. Liu [b,*], L. Bascetta [a], E. De Momi [a], P. Poignet [b]

[a] *Department of Electronics, Information and Bioengineering (DEIB), Politecnico di Milano, Piazza Leonardo da Vinci 32, 20133 Milano, Italy* [b] *Department of Robotics, LIRMM (UMR5506), UM-CNRS, 161 Rue Ada, 34095 Montpellier, France*

In minimally invasive surgery (MIS) the continuously increasing use of robotic devices allows surgical operations to be conducted more precisely and more efficiently. Safe and accurate interaction between robot instruments and living tissue is an important issue for both successful operation and patient safety. Human tissue, which is generally viscoelastic, nonlinear and anisotropic, is often described as purely elas-tic for its simplicity in contact force control design and online computation. However, the elastic model cannot reproduce the complex properties of a real tissue. Based on *in vitro* animal tissue relaxation tests, we identify the Hunt–Crossley viscoelastic model as the most realistic one to describe the soft tissue's mechanical behavior among several candidate models. A force control method based on Hunt–Crossley model is developed following the state feedback design technique with a Kalman filter based active observer (AOB). Both simulation and experimental studies were carried out to verify the performance of developed force controller, comparing with other linear viscoelastic and elastic model based force con-trollers. The studies and comparisons show that the Hunt–Crossley model based force controller ensures comparable rise time in transient response as the controller based on Kelvin–Boltzmann model which is reported as the most accurate description for robot-tissue interaction in recent literature, but it causes much less overshoot and remains stable for tasks with faster response time requirements.

Keywords:
Force control
Soft tissue interaction
Active observer
Hunt–Crossley model

1. Introduction

Minimally invasive surgery (MIS) is replacing traditional open surgical procedures which normally involve large incision to access the patient's body. MIS is performed using long instruments to enter the patient body through small incisions and leads to direct advantages including less pain, hemorrhaging and trauma, reduced risk of infections, shortened hospital stay, and hence less burden for both the patient and social health care system [1–3].

With the development of technology in the area of robotics, robotic devices have found their way to the operating room (OR) and lead to the new concept of minimally invasive robotic surgery (MIRS). Many robotic surgical devices have been developed for MIS operations in the literature [4–9] with the most widely used and best known example of da Vinci robot from Intuitive Surgical (Sunnyvale, CA, USA). The movements of the robotic devices, commanded by the surgeon, can mimic the motion of human hands inside patient body to accomplish safer and more precise operations. However, as pointed out in [10], the surgeon can not retain the haptic feeling of the interaction with tissue due to lack of direct contact with the working site and hence the amount of applied force on tissue surface cannot be accurately controlled.

Execution of proper contact force is necessary and even essential for many surgical operations [11–13]. For tasks like suturing and pre-tensioning, excessive force leads to tissue damage and too low force cannot make the tasks successful. For haptic teleoperation with force command, operating transparency can be obtained only when the desired interaction force is accurately generated between robotic tool and tissue. Moreover, using force control allows to perform the same operation with higher precision and dexterity by reducing human errors [14].

In the MIRS scenario, one has to control the contact force between robotic surgical tools and soft tissues (i.e. muscles, organs, veins, arteries, etc). To design the force controller, a proper tool-tissue contact model is required. In literature, however, force control methods are mainly based on pure elastic contact model which is easy to implement and applies to most hard contact cases.

* Corresponding author. Tel.: +33 685817659.
E-mail addresses: pappalardo.antonio87@gmail.com (A. Pappalardo), Abdulrahman.Albakri@lirmm.fr (A. Albakri), Chao.Liu@lirmm.fr (C. Liu), luca.bascetta@polimi.it (L. Bascetta), elena.demomi@polimi.it (E. De Momi), Philippe.Poignet@lirmm.fr (P. Poignet).

©2016. This manuscript version is made available under the CC-BY-NC-ND 4.0 license http://creativecommons.org/licenses/by-nc-nd/4.0/
Published Journal Article available at: http://dx.doi.org/10.1016/j.bspc.2016.05.003

Even some existing works on force control for surgical applications assume an elastic contact model [15]. Unfortunately, this model is not suitable to describe the contact with soft human tissues which exhibits complex properties such as nonlinearity, viscoelasticity, anisotropy, etc [16].

Over the last decades, several compliant contact models have been proposed to describe the behavior between contact bodies [17]. Combination of linear springs and dampers is one way to describe the viscoelastic behavior of the contact force, although these approaches show physical inconsistencies in terms of power exchange during contact [18]. Such kind of linear contact models include Maxwell model, Kevin–Voigt model, Kelvin–Boltzmann model, etc. Recent works show that robot-tissue force control based on Kelvin–Boltzmann model outperforms control methods based on traditional elastic model in terms of rise time and stability [19]. On the other hand, nonlinear models, such as the Hunt–Crossley model, are expected to be more accurate for describing the real behavior during the contact with soft human tissues [18,20]. However, so far nonlinear models have only been used for parameter estimation [18,21,22], but not for force control design.

This paper presents the first attempt to adopt the Hunt–Crossley (HC) model for the control design of contact force between soft tissue and robotic tool in literature. The control design utilizes the active observer (AOB) technique which helps to compensate parameter and modeling mismatches during control. Stability of the HC model based force control system is analyzed, and the advantage of this approach with respect to the methods based on linear contact models is shown through both numerical simulation and *in vitro* experimental studies.

The rest of the paper is organized as follows: Section 2 introduces the brief background on soft tissue contact models reported in literature; Section 3 presents a comparison study between linear and nonlinear viscoelastic contact models through *in vitro* relaxation tests, Section 4 describes the development of a force control method based on the identified Hunt–Crossley model, Sections 5 and 6 show the performance comparisons between linear con-tact model based force controllers and Hunt–Crossley model based force controller through simulations and experiments, Section 7 summarizes the work reported in this paper.

2. Soft tissue contact models

Several models have been developed in literature to describe the viscoelastic behavior of soft tissues [23]. The most complete study on viscoelastic tissue model is addressed in [16], where a quasi-linear viscoelastic (QLV) model is proposed to represent the stress–strain relationship as follows

$$F(t) = \underbrace{G(t)\sigma^e[\varepsilon(0)]}_{I} + \underbrace{\int_0^t G(t-\tau)\frac{\partial \sigma^e(\tau)}{\partial \tau}d\tau}_{II} \quad (1)$$

where $F(t)$ denotes the contact force; σ^e, ε denotes the instantaneous elastic stress and strain respectively; $G(t)$ is the reduced relaxation modulus. This modeling function is composed of two parts: the first part (I) is the instantaneous stress response and the second (II) gives the stress related to the past history [16]. Although accurate for off-line analysis, this model is complex and difficult to be used for contact force control design.

One simple and intuitive way to describe the interaction between robotic tools and soft tissues is to analytically build the force–displacement relationship. Analytical models are usually presented as a combination of springs and dampers [16], and are defined by the following components: the exerted force by the tissue, $F_e(t)$, when a strain is applied; the indentation (or penetration), $x(t)$, computed as the amount of displacement of the tissue from the rest position; the velocity of the deformation $\dot{x}(t)$; the elastic and damping coefficients K and b respectively.

Following this modeling method, several linear models have been developed. The first model, often used in traditional force control [24], is the elastic model (Fig. 1(a)) described by

$$F_e(t) = Kx(t). \quad (2)$$

The Maxwell (MW) model is represented by the series of a spring and a damper (Fig. 1(b)) and is expressed as

$$F_e(t) = b\dot{x}(t) - \alpha\dot{F}_e(t) \quad (3)$$

where $\dot{F}_e(t)$ is the derivative of the exerted force and $\alpha = b/K$.

The Kelvin–Voigt (KV) model consists of a spring in parallel with a damper (Fig. 1(c)) and is described by

$$F_e(t) = Kx(t) + b\dot{x}(t). \quad (4)$$

Another viscoelastic model is the Kelvin–Boltzmann (KB) model which is obtained by adding a spring in series to Kelvin–Voigt model (Fig. 1(d)) and its characteristic equation is given by

$$F_e(t) = Kx(t) + \eta\dot{x}(t) - \gamma\dot{F}_e(t) \quad (5)$$

where $K = k_1k_2/(k_1 + k_2)$, $\eta = bk_2/(k_1 + k_2)$, $\gamma = b/(k_1 + k_2)$ with k_1, k_2 and b denoting the elastic and damping coefficients respectively.

The above linear models may apply to contacts with objects of linear and homogeneous properties, but physical limitations can be observed when contact with soft tissue is considered. As illustrated in Fig. 2, during the contact between a rigid tool and the soft tissue, two phases can be identified: the first one, corresponding to load-ing, takes place at starting contact time t_0 and ends at t_{Max} when the maximum displacement in the soft tissue x_{max} is reached; the second one, corresponding to unloading, takes place from t_{max} to the instant t_{Final} when the tool and the soft tissue separate. Combining the loading and unloading behavior, an hysteresis loop can be defined as the force–displacement relationship for soft tissue during the contact.

The power flow during the contact is calculated by $P(t) = F_e(t)\dot{x}(t)$ as plotted on the right side of each subfigure in Fig. 3. For linear viscoelastic models, the dissipated energy ΔH, represented by the area enclosed by the hysteresis loop, can be computed as the algebraic sum of the energies H_1, H_2 and H_3, which are calculated as integrations of power flow for different periods as shown in Fig. 3(a) [18]. Linear viscoelastic models show the same behaviors

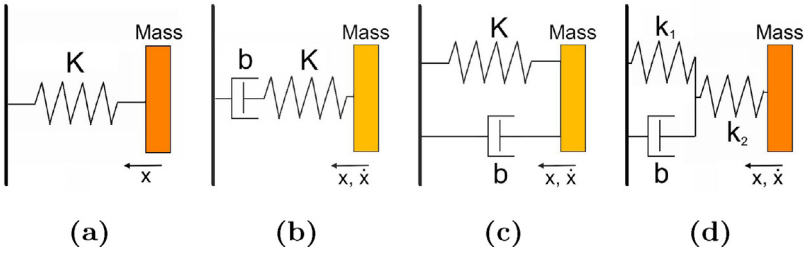

Fig. 1. Linear contact models: (a) elastic, (b) Maxwell, (c) Kelvin–Voigt, (d) Kelvin–Boltzmann.

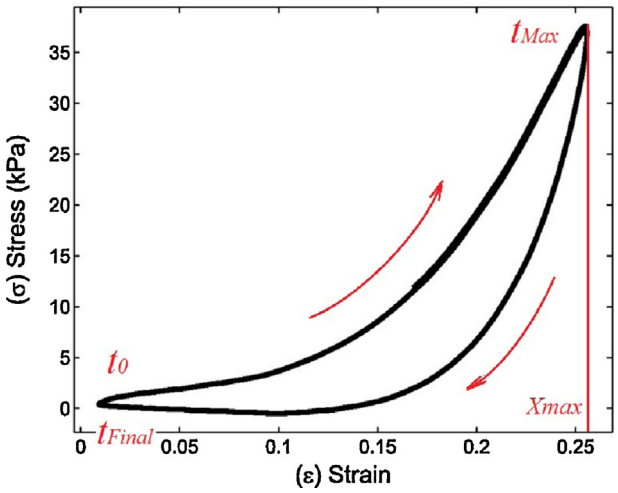

Fig. 2. Stress–strain curve (hysteresis) for selected section of laryngeal muscle [25].

as in Fig. 3(a) with only difference in shapes. It can be seen that linear viscoelastic models show inconsistencies against physical intuition in two aspects [20,18]. The first one concerns the con-tact force when the soft tissue surface just starts to deform (time t_0). Physically the interaction force should start from zero and then build up over time, but a non-zero force is observed at the beginning due to the damping terms [26]. The second is caused by the tensile forces required to separate the bodies in contact. In the unloading phase the displacement $x(t)$ decreases to zero and the velocity $\dot{x}(t)$ is negative. For this phase, linear viscoelastic models indicate the existence of a positive energy H_3 meaning that power still flows from the end-effector to the tissue after separation, which is physically impossible [18].

To address the aforementioned problems with linear viscoelastic models, Hunt and Crossley proposed in [20] a new model. Replacing the spring/damper linear combination in (4) with a non-linear one, the obtained model equation is given by

$$F(t) = Kx^{\beta}(t) + \lambda x^{\beta}\dot{x}(t) \tag{6}$$

where β is a positive scalar and normally ranges from 1.1 to 1.3 for soft tissues. The main characteristic of the Hunt–Crossley (HC) model is the effect of deformation depth on the damping term. With the HC model, the contact force evolves from zero reaching the maximum value during the loading phase and returns to zero dur-ing the unloading phase. Accordingly, a physically correct power flow is seen as in Fig. 3(b).

3. Soft tissue contact model identification and parameter estimation

Starting from the models described in the previous section (Table 1), experimental tests based on *in vitro* tissue samples have been carried out in order to assess their accuracy in describing the contact force-deformation relationship.

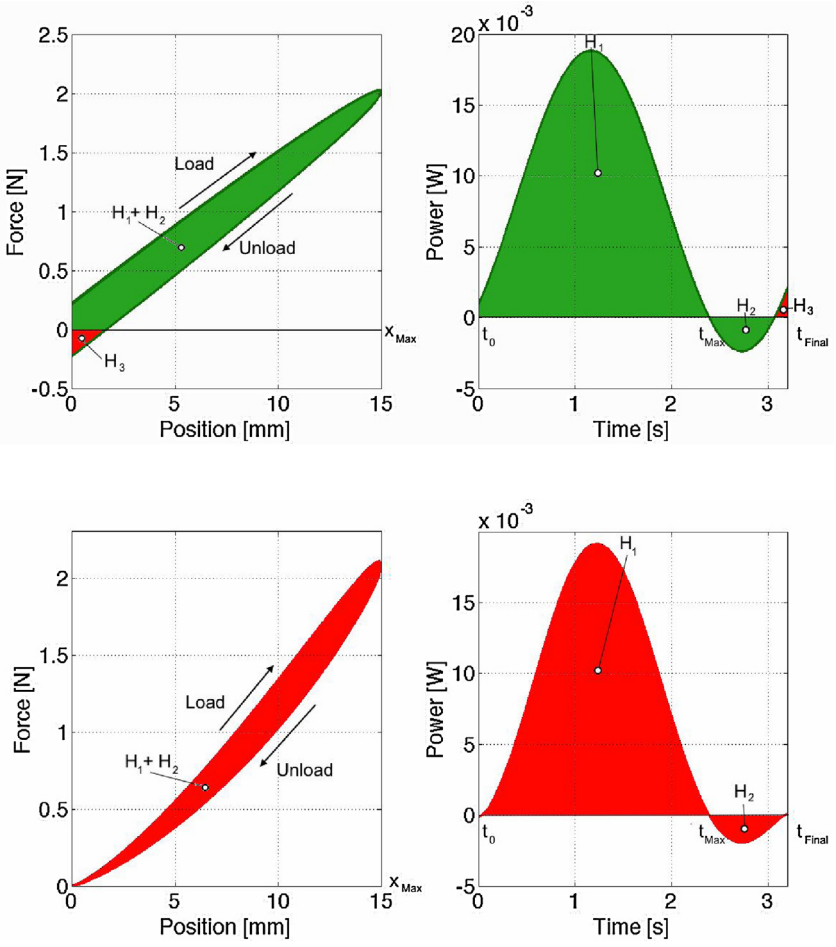

Fig. 3. Force–displacement hysteresis and power flow during contact: (a) linear contact model (Kelvin–Voigt, Kelvin–Boltzmann, Maxwell model), (b) Hunt–Crossley model.

Table 1
Candidate models.

Model	Constitutive law
Elastic	$F(t) = Kx(t)$
MW	$F(t) = b\dot{x}(t) - \alpha\dot{F}(t)$
KV	$F(t) = Kx(t) + b\dot{x}(t)$
KB	$F(t) = Kx(t) + \eta\dot{x}(t) - \gamma\dot{F}(t)$
HC	$F(t) = Kx^{\beta}(t) + \lambda x^{\beta}(t)\dot{x}(t)$

3.1. Relaxation test design

In order to analyze the relationship between tissue deformation and reacting force, it is common to perform relaxation tests on *in vitro* specimens. The relaxation test consists of generating a fixed deformation along the direction normal to the tissue surface and measuring the corresponding force exerted by the tissue. Force and deformation depth data are saved to off-line estimate the param-eters of candidate models and thus to calculate the reconstructed force based on different models using recorded deformation data.

In this relaxation test, a lamb's heart is used as the *in vitro* specimen and a RAVEN-II surgical robot is used to generate the tissue deformation as explained in detail in next subsection. The test has been run four times to verify consistency of the observed tissue interaction property. To identify the most accurate (realis-tic) model to describe soft tissue interaction, both transient and overall force reconstruction errors are considered as selection crite-ria. The experiment results are evaluated by comparing the mean force error (MFE) and corresponding standard deviation (STD) of the reconstructed forces for each model, and Kruskal–Wallis test ($p < 0.05$) is used to investigate the significant differences between different model-based force reconstruction errors.

3.2. Relaxation test execution

The Raven-II surgical robot from Applied Dexterity (Seattle, WA, USA) was used for the relaxation tests as shown in Fig. 4. The robot platform is running a Real-Time Linux system with an overall system working frequency of 1 kHz. This robot is composed of two cable-actuated arms and each has seven degrees of freedom, which creates a spherical mechanism that allows dexterous tool manipulation within a large workspace similar to that of manual laparoscopy [28].

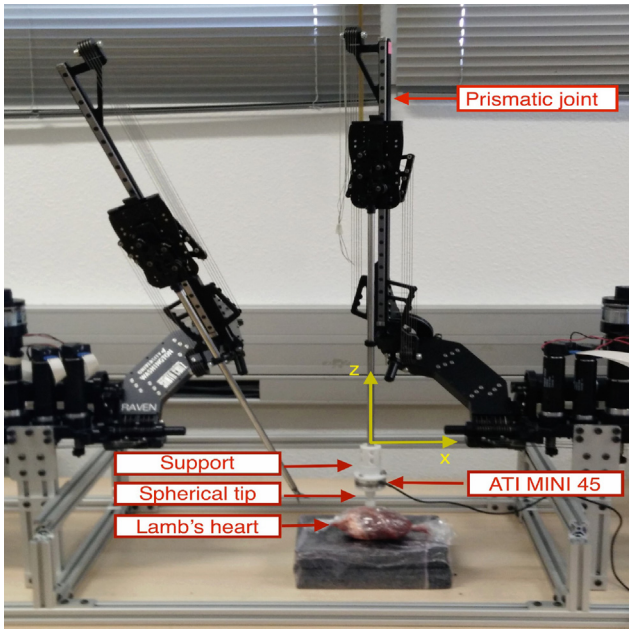

Fig. 4. Relaxation test using Raven II robot.

In the relaxation tests, the involved joint is the prismatic one of the right arm. As shown in Fig. 4, this arm was set in vertical configuration (along z axis) and a PID position control was used to generate the vertical motion to deform the tissue sample. The motion data were recorded by the prismatic joint encoder which is of high accuracy and no external position sensor was used. The exerted force data were collected by an ATI MINI45 force sensor (ATI Industrial Automation, Apex, NC) mounted on the wrist joint of the robot by a 3D printed plastic support with a spherical tip. The data were recorded with a sampling period T_s of 1 ms (1 kHz).

Four relaxation tests were performed. Before the relaxation test, the robot instrument was controlled to move down from free space (no contact) until the detected contact force increased by 0.5 N above the baseline value (0 N) to ensure real contact between the robot tip and the tissue. Then the PID position control was triggered to generate a displacement depth of 15 mm from the initial surface with the ramp up time of 0.5 s and loading time of 20 s. In order to observe the hysteresis behavior, the unloading was also done with a ramp down time of 1 s. Fig. 5(a) shows the recorded displacement-force history of one test (Trial 3).

3.3. Parameter estimation

Based on the saved data for position $x(t)$ and force measurement $F(t)$, off-line least squares method is used to estimate the parame-ters K, b, η, α, γ of the linear contact models (elastic, MW, KV, KB).$\dot{x}(t)$ and $\dot{F}(t)$ are calculated based on filtered position and force data using moving average technique.

For the nonlinear HC model, the estimated parameters K, λ, β are calculated through nonlinear least squares method using the Levenberg–Marquardt algorithm [29,30]. The estimated parameters for the candidate models in the four tests are summarized in Table 2.

3.4. Model identification based on reconstructed force

With the estimated parameters, the contact force can be reconstructed based on the recorded position information using different model. Since all four tests generated similar results, only the reconstructed forces corresponding to Trial 3 are shown in Fig. 5.

Graphical inspection of the reconstructed forces as in Fig. 5(b) shows that all models give rise to the same descriptions for steady state contact forces except the Maxwell model, which presents a totally unrealistic reconstructed force (zero static contact force) and therefore is not considered in the further comparison and analysis. As shown in Fig. 5(c), the pure elastic model clearly shows the worst reconstructed force. The reconstructed transient responses

Table 2
Values of the estimated parameters.

Model	Parameter	Mean	STD	STD/mean [%]
Elastic	K	628.92	14.11	2.24
MW	b	349.58	13.39	3.83
	α	0.27	0.01	3.70
KV	K	629.11	14.11	2.24
	b	112.72	9.10	8.07
KB	K	636.05	16.21	2.55
	η	156.92	4.10	2.61
	γ	0.052	0.0046	8.85
HC	K	1,732.23	275.82	15.92
	λ	41,891.57	1,314.90	3.14
	β	1.23	0.03	2.44

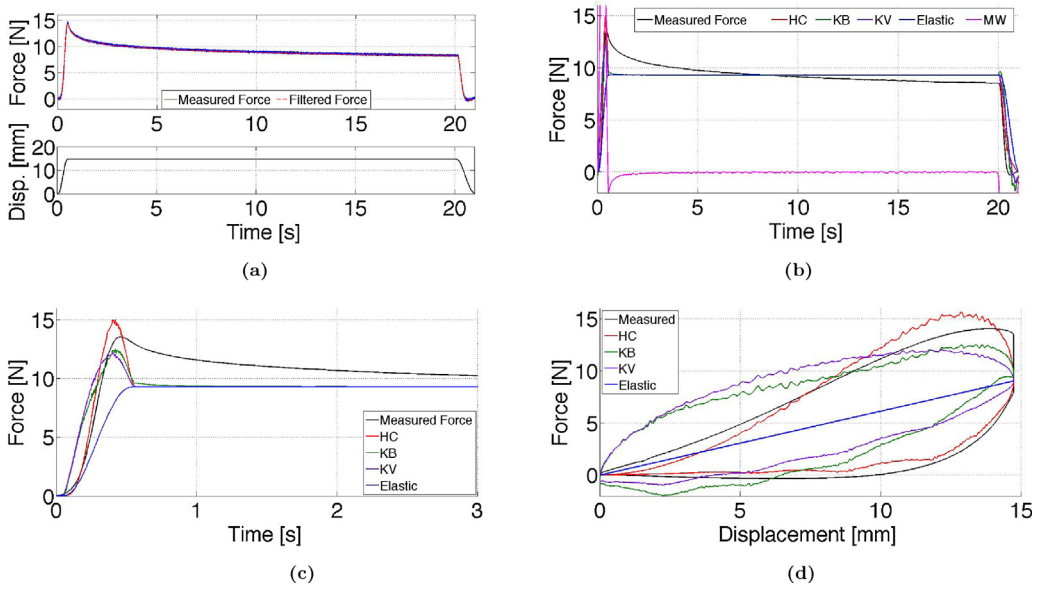

Fig. 5. Reconstructed forces for the Trial 3: (a) ramp deformation and force measurement, (b) reconstructed forces, (c) zoomed in reconstructed transient responses, (d) reconstructed hysteresis behaviors.

Table 3
Average values of MFE [N] and STD [N] for the four relaxation tests.

Model	MFE	STD
Elastic	0.80	0.98
KV	0.72	0.73
KB	0.71	0.71
HC	0.65	0.58

for the linear viscoelastic models (KV, KB) are similar and show a lead in phase compared to the real measured force at the beginning of contact. The Hunt–Crossley model shows a quite accurate reconstructed transient response as the real force.

The MFE and STD of reconstructed forces according to different contact models are calculated and summarized in Table 3. As shown in this table, the Hunt–Crossley model exhibits the smallest mean error and standard deviation. Kruskal–Wallis test ($p < 0.05$) with the null hypothesis "*the reconstruction errors with different interaction models follow the same distribution*" has been conducted and the test results are shown in Table 4.

From Table 4 it is seen that the null hypothesis is false with all p-values $p \ll 1\,\%$ and therefore the four interaction models do not produce the same distributions of reconstructed force errors with the Hunt–Crossley model presenting the smallest mean error. To further clarify if there is any model which may generate reconstruction error with the same distributions as Hunt–Crossley model, Kruskal–Wallis analysis has also been conducted as summarized in Table 5.

Above analyses show that Hunt–Crossley model gives significantly smaller reconstructed contact force error with respect to the other linear interaction models. It should be noted that the above analyses are for the whole relaxation test duration including both the transient response reconstruction and the steady state reconstruction. From the zoomed in transient contact response as in Fig. 5(c), it is seen that all reconstructed forces based on different models converge to the same value in less than 1 s (same for all four tests), hence only reconstruction errors between 0 and 0.8 s (transient response) are considered to avoid misleading results due to the large amount of data for steady state with almost the same values (after 0.8 s) such that the significance of validation tests is clearer. The notched box whisker method is used to illustrate the reconstructed force errors in all four tests during 0–0.8 s as shown in Fig. 6. It is seen from this figure that there is strong evidence (95%) that the force reconstruction error of Hunt–Crossley model has a different median from other models since its box's notch does not overlap with any other model. And it is clearly shown that the median for Hunt–Crossley model is smaller than other models indicating that Hunt–Crossley model provides more accurate force reconstruction in the validation test.

Moreover, the reconstructed loading and unloading behaviors of the candidate models are also shown in Fig. 5(d). The linear viscoelastic models (KV, KB) predict negative contact forces in the unloading phase and the Hunt–Crossley model shows a realistic hysteresis behavior, which is consistent with the physical interpretations as introduced in Section 2.

Therefore, through the *in vitro* relaxation tests, Hunt–Crossley model has been identified as the most accurate one among all candidate models to describe the interaction between the robot's end-effector and the soft tissue.

Table 4
p-value for the four relaxation tests.

	Test 1	Test 2	Test 3	Test 4
p-value	$7.7451e^{-12}$	$6.6636e^{-05}$	$3.3294e^{-12}$	$3.6771e^{-13}$

Table 5
Kruskal–Wallis analysis for each test.

		HC (p-value)
Test 1	Elastic	$3.4060e^{-10}$
	KV	$1.5193e^{-10}$
	KB	$1.8489e^{-06}$
Test 2	Elastic	0.0108
	KV	$1.3866e^{-07}$
	KB	$8.8199e^{-07}$
Test 3	Elastic	$1.2584e^{-04}$
	KV	$8.3806e^{-12}$
	KB	$2.3771e^{-10}$
Test 4	Elastic	0.0178
	KV	$1.0167e^{-08}$
	KB	$3.2448e^{-13}$

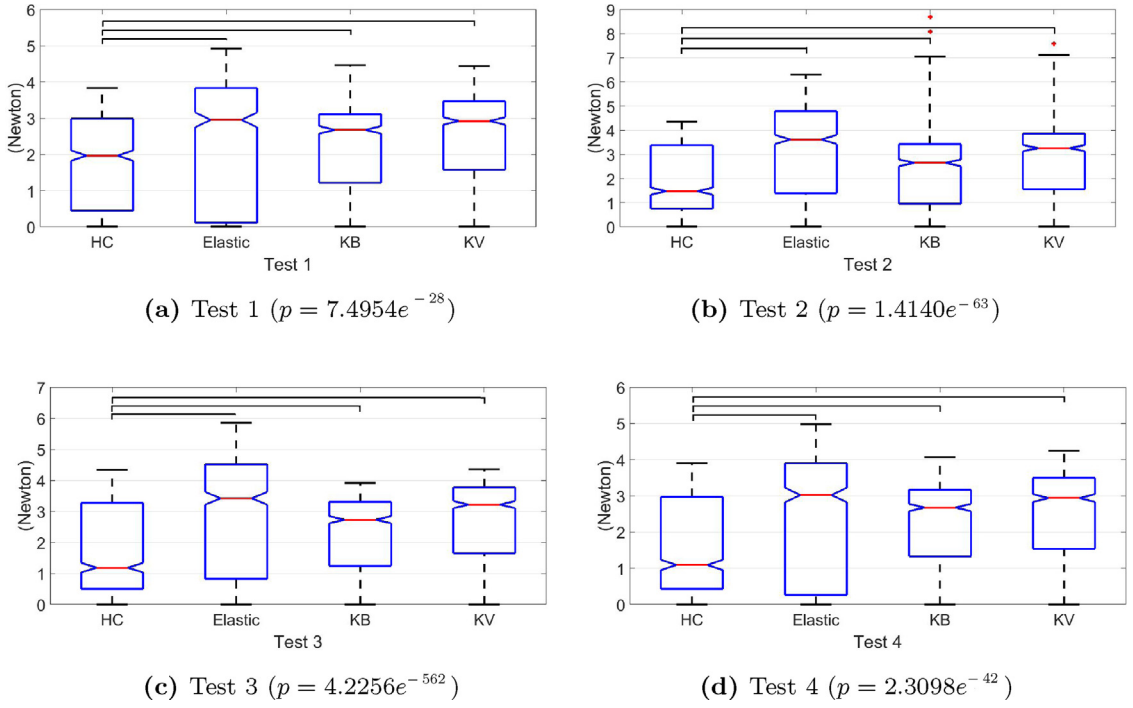

(a) Test 1 ($p = 7.4954e^{-28}$) **(b)** Test 2 ($p = 1.4140e^{-63}$)

(c) Test 3 ($p = 4.2256e^{-562}$) **(d)** Test 4 ($p = 2.3098e^{-42}$)

Fig. 6. Evaluation of force reconstruction errors (0–0.8 s) for all four test with their p-values respectively. The vertical boxes show median values (in red) and quartiles (25% as box lower limit and 75% as box upper limit) of the reconstructure error datasets. The horizontal lines represent significant differences between Hunt–Crossley and other models determined through comparisons (Kruskal–Wallis test, $p < 0.05$). (For interpretation of the references to color in this figure legend, the reader is referred to the web version of this article.)

4. Hunt–Crossley model based force control

For surgical applications, linear control methods are normally preferred since there exist mature analysis and design tools for linear systems. Also, clear and simple relation can be established between system performance specifications and the control parameters. On the contrary, in general no uniform tools exist for nonlinear system control design, and it is difficult to relate controller design to pre-defined performance specifications, e.g. rise time, phase/gain margin, etc.

To synthesize the force controller using linear design tools based on Hunt–Crossley model, this model has to be linearized. In this work, the force control is designed resorting to state feedback regulation with a stochastic Kalman filter based active observer (AOB), whose role is to estimate the states of the system and compensate for modeling errors (e.g. linearization) and system disturbances through an extra "active" state.

4.1. Linearization of nonlinear Hunt–Crossley model

Considering that during contact the tissue deformation is fast (transient state) and then keeps almost constant ("steady" state), as can be seen from Fig. 5(b), it is reasonable to linearize the Hunt–Crossley model around the "steady" state which is the equilibrium position x_s for a given desired force command F_d as seen in Fig. 7

Using Taylor expansion, the corresponding first-order linearized Hunt–Crossley model at $x = x_s$ has the following expression

$$F_e(x, \dot{x}) \approx F_e(x_s, \dot{x}_s) + \left.\frac{\partial F_e}{\partial x}\right|_{x_s,\dot{x}_s} (x - x_s) + \left.\frac{\partial F_e}{\partial \dot{x}}\right|_{x_s,\dot{x}_s} (\dot{x} - \dot{x}_s). \tag{7}$$

For a given desired force, F_d, from Eq. (6) the constant equilibrium position x_s can be calculated from

$$F_d = F_e(x_s, \dot{x}_s) = Kx_s^{\beta} + \lambda x_s^{\beta}\dot{x}_s = Kx_s^{\beta}, \tag{8}$$

giving rise to

$$x_s = \sqrt[\beta]{\frac{F_d}{K}}. \tag{9}$$

The partial derivative terms $\partial F_e/\partial x$ and $\partial F_e/\partial \dot{x}_s$ at x_s and $\dot{x}_s$ in (7) can then be calculated using (9) as

$$\begin{aligned} \left.\frac{\partial F_e}{\partial x}\right|_{x_s,\dot{x}_s} &= K\beta x_s^{\beta-1} + \lambda\beta x_s^{\beta-1}\dot{x}_s = \overbrace{K\beta\left(\frac{F_d}{K}\right)^{(\beta-1)/\beta}}^{\tilde{K}} \\ \left.\frac{\partial F_e}{\partial \dot{x}}\right|_{x_s,\dot{x}_s} &= \lambda x_s^{\beta} = \overbrace{\lambda\frac{F_d}{K}}^{\tilde{\lambda}} \end{aligned}. \tag{10}$$

Substituting (10), (9) into (7), the linearized function of the Hunt–Crossley model for the given desired force F_d can be obtained as

$$F_e(x, \dot{x}) = \tilde{K}x + \tilde{\lambda}\dot{x} + (1 - \beta)F_d. \tag{11}$$

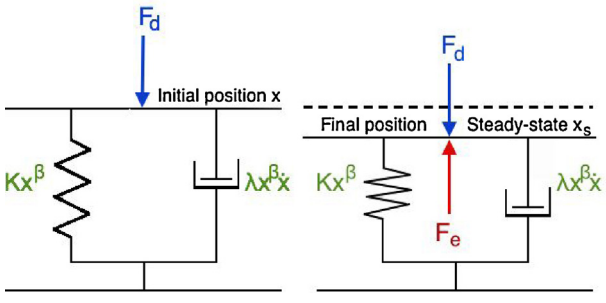

Fig. 7. Equilibrium position of Hunt–Crossley model for a desired force F_d.

The neglected high order terms would be considered as modeling errors and handled by the active state of AOB.

4.2. Robot dynamics and control system formulation

The joint space dynamics of a robot, with n degrees of freedom and joint variables denoted by q, can be written in the following form [24]

$$M(q)\ddot{q} + V(q,\dot{q}) + G(q) = \tau_c - J^T(q)F_e \tag{12}$$

where $M(q)$ is the robot inertia matrix, $V(q,\dot{q})$ represents Coriolis and centrifugal forces, $G(q)$ is the gravity force vector and τ_c represents the generalized torque input. F_e denotes the interaction forces due to contact with the environment and $J(q)$ is the Jacobian matrix mapping joint space velocity $\dot{q}$ to Cartesian space velocity $\dot{X}$ as

$$\dot{X} = J(q)\dot{q}. \tag{13}$$

The robot dynamics in Cartesian space can be equally obtained as [27,24]

$$M_x(q)\ddot{X} + V_x(q,\dot{q}) + G_x(q) = F_c - F_e \tag{14}$$

where X represents the Cartesian coordinates, F_c is the end-effector force due to joint actuation as

$$\tau_c = J^T(q)F_c \tag{15}$$

and the matrices in (14) are given by

$$\begin{aligned} M_x(q) &= J^{-T}(q)M(q)J^{-1}(q) \\ V_x(q,\dot{q}) &= J^{-T}(q)V(q,\dot{q}) - M_x(q)\dot{J}(q)\dot{q} \\ G_x(q) &= J^{-T}(q)G(q). \end{aligned}$$

Assuming that the above matrices can been accurately identified and a force sensor is available to measure F_e, the robot dynamics (14) can be linearized using the following inverse-dynamics control input

$$F_c = M_x(q)U + V_x(q,\dot{q}) + G_x(q) + F_e. \tag{16}$$

where U represents the auxiliary control signal. In cases where the system dynamics parameters cannot be accurately calibrated, adaptive compensation technique could be used in the control design.

Substituting (16) in (14), the system becomes

$$U = \ddot{X} \tag{17}$$

presenting a decoupled unity mass system along each Cartesian dimension. By adding an inner velocity damping loop with diagonal matrix K_v, the system stability can be improved [31]. The new dynamics equation is given by

$$U = \ddot{X} + K_v\dot{X}. \tag{18}$$

Now that the system is decoupled, each degree of freedom can be independently expressed as

$$U_i = \ddot{X}_i + K_v\dot{X}_i \tag{19}$$

where $\ddot{X}_i$ and $\dot{X}_i$ represent the acceleration and the velocity along one axis, and U_i is the auxiliary control input. The general system block diagram is presented in Fig. 8.

Differentiating the linearized Hunt–Crossley soft tissue model in (11) and noting that F_d is constant, one obtains

$$\dot{F}_e = \tilde{K}\dot{X}_i + \tilde{\lambda}\ddot{X}_i, \quad \ddot{F}_e = \tilde{K}\ddot{X}_i + \tilde{\lambda}\dddot{X}_i \tag{20}$$

and according to the decoupled dynamics equation (18), it follows

$$\dot{U}_i = \dddot{X}_i + K_v\ddot{X}_i. \tag{21}$$

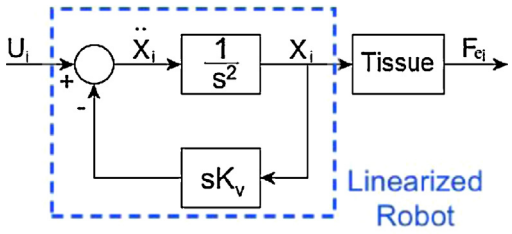

Fig. 8. System diagram for one Cartesian axis.

From Eqs. (19), (20) and (21), the relationship between contact force F_e and control input U_i along one axis can be written as

$$\ddot{F}_e + K_v\dot{F}_e = \tilde{\lambda}\dot{U}_i + \tilde{K}U_i. \tag{22}$$

Based on (22), the transfer function $G(s)$ describing the relation between the control input U_i and F_e can be given by

$$G(s) = \frac{F_{ei}(s)}{U_i(s)} = \frac{\tilde{\lambda}s + \tilde{K}}{s^2 + K_v s}. \tag{23}$$

The system in (22) can be represented in state space form as well based on its transfer function (23). Using the observable canonical form [33], one obtains

$$\begin{aligned} \begin{bmatrix} \dot{x}_1 \\ \dot{x}_2 \end{bmatrix} &= \begin{bmatrix} -K_v & 1 \\ 0 & 0 \end{bmatrix} \begin{bmatrix} x_1 \\ x_2 \end{bmatrix} + \begin{bmatrix} \tilde{\lambda} \\ \tilde{K} \end{bmatrix} u = Ax + Bu \\ y(t) &= \begin{bmatrix} 1 & 0 \end{bmatrix} \begin{bmatrix} x_1 \\ x_2 \end{bmatrix} = Cx. \end{aligned} \tag{24}$$

For practical implementation, system (24) is often discretized using zero order hold (ZOH) with a sample time T_s. Then the discrete state space representation is given by

$$\begin{aligned} x(k) &= \Phi x(k-1) + \Gamma u(k-1) + \omega(k) \\ y(k) &= Cx(k) + \eta(k) \end{aligned} \tag{25}$$

where Φ, Γ are the discrete state matrix and the discrete input matrix respectively, and two additional terms ω, η are introduced to denote the model and measurement uncertainties in real practice.

The discrete state matrices were obtained as [32]

$$\begin{aligned} \Phi &= e^{AT_s} = I + AT_s + \frac{A^2T_s^2}{2!} + \frac{A^3T_s^3}{3!} + \dots \\ \Gamma &= \int_0^{T_s} e^{AT_s}Bd\tau = BT_s + AB\frac{T_s^2}{2!} + A^2B\frac{T_s^3}{3!} + \dots \end{aligned} \tag{26}$$

where A, B are the matrix defined in (24) and I is the identity matrix.

The control law can be designed following the state feedback regulation method as

$$u(k) = -Lx(k) + r(k) \tag{27}$$

where $r(k)$ is the reference force (F_d) and L is the state feedback gain which can be calculated according to pole placement technique using the Ackermann's formula [32].

4.3. Active observer based on Kalman filter

It should be noted that control law (27) needs full system state information which is difficult to achieve since the system state $x(k)$ in (25) may not have clear physical interpretation and cannot be directly measured. In this case, an observer is usually the natural solution. The role of the classical observer is to compute the estimated system state $\hat{x}(k)$ based on the system equations and output measurements. Kalman filter is a popular technique to achieve this objective in practice.

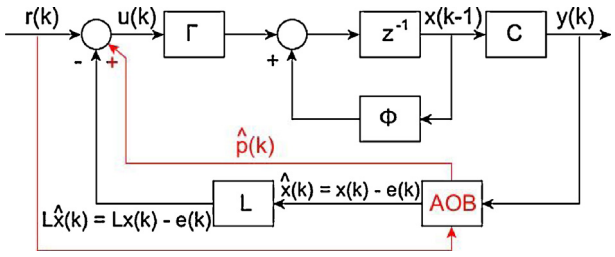

Fig. 9. Force control architecture.

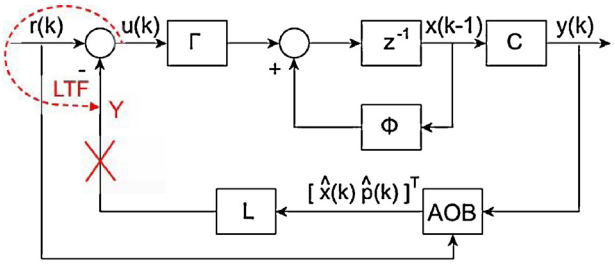

Fig. 10. Loop transfer function.

In real application, there exists an error $e(k)$ between the estimated state and the actual state as follows

$$e(k) = x(k) - \hat{x}(k). \tag{28}$$

One can notice that when state feedback is performed in combination with an observer, the error in (28) is introduced in the system as an undesired extra input as follows

$$L\hat{x}(k) = Lx(k) - Le(k). \tag{29}$$

Traditional Kalman filters cannot solve this system state observation/reconstruction error problem. In this work, a Kalman filter based active observer (AOB) technique is used to handle the state observation error. Different from traditional Kalman filters, the goal of the active observer, as shown in Fig. 9, is to estimate and com-pensate this error by using a feedforward term based on an extra state, also called as active state $p(k)$, given by [34,35]:

$$p(k) = Le(k). \tag{30}$$

According to [35], a stochastic approach is used to model $p(k)$ as

$$p(k) - p(k-1) = \xi(k) \tag{31}$$

where $\xi(k)$ is a zero-mean Gaussian random variable and is used in Kalman equation, by the AOB algorithm, as a white noise to describe the evolution of $p(k)$ [35].

Rewriting Eq. (25) by taking into account the extra state $p(k)$, the discrete state space description becomes

$$\begin{aligned} \begin{bmatrix} x(k) \\ p(k) \end{bmatrix} &= \begin{bmatrix} \Phi & \Gamma \\ 0 & 1 \end{bmatrix} \begin{bmatrix} x(k-1) \\ p(k-1) \end{bmatrix} + \begin{bmatrix} \Gamma \\ 0 \end{bmatrix} u\prime(k-1) + \begin{bmatrix} \omega(k) \\ \xi(k) \end{bmatrix} \\ y(t) &= C_a \begin{bmatrix} x(k) \\ p(k) \end{bmatrix} + \eta(k) \end{aligned} \tag{32}$$

with the augmented control input

$$u\prime(k-1) = r(k-1) - \begin{bmatrix} L & 1 \end{bmatrix} \begin{bmatrix} x(k-1) \\ p(k-1) \end{bmatrix}$$

and $C_a = [\, C \quad 0 \,]$.

Then the closed loop system can be written as

$$\begin{bmatrix} x(k) \\ p(k) \end{bmatrix} = \begin{bmatrix} \Phi - \Gamma L & 0 \\ 0 & 1 \end{bmatrix} \begin{bmatrix} x(k-1) \\ p(k-1) \end{bmatrix} + \begin{bmatrix} \Gamma \\ 0 \end{bmatrix} r(k-1) + \begin{bmatrix} \omega(k) \\ \xi(k) \end{bmatrix} \tag{33}$$

and the active observer based on (33) is given by

$$\begin{aligned} \begin{bmatrix} \hat{x}(k) \\ \hat{p}(k) \end{bmatrix} &= \begin{bmatrix} \Phi - \Gamma L & 0 \\ 0 & 1 \end{bmatrix} \begin{bmatrix} \hat{x}(k-1) \\ \hat{p}(k-1) \end{bmatrix} \\ &\quad + \begin{bmatrix} \Gamma \\ 0 \end{bmatrix} r(k-1) + K(k)(y(k) - \hat{y}(k)) \end{aligned} \tag{34}$$

where

$$\hat{y}(k) = C_a \left(\begin{bmatrix} \Phi - \Gamma L & 0 \\ 0 & 1 \end{bmatrix} \begin{bmatrix} \hat{x}(k-1) \\ \hat{p}(k-1) \end{bmatrix} + \begin{bmatrix} \Gamma \\ 0 \end{bmatrix} r(k-1) \right).$$

The Kalman filter gain $K(k)$ is calculated using the following equations

$$\begin{aligned} K(k) &= P_1(k) C_a^T [C_a P_1(k) C_a^T + R(k)]^{-1} \\ P_1(k) &= \Phi_a P(k-1) \Phi_a^T + Q(k) \\ P(k) &= P_1(k) - K(k) C_a P_1(k) \end{aligned} \tag{35}$$

with

$$\Phi_a = \begin{bmatrix} \Phi & \Gamma \\ 0 & 1 \end{bmatrix}, \quad Q(k) = \begin{bmatrix} Q_{x(k)} & 0 \\ 0 & Q_{p(k)} \end{bmatrix}$$

where the matrix Φ_a is the augmented open loop matrix, $Q(k)$ is the process covariance matrix and $R(k)$ is the measurement covariance noise. The covariance $Q_{p(k)}$ is related to the effectiveness of active state $\hat{p}(k)$ to compensate the errors. The higher this value is, the more effective the error compensation will be.

4.4. System stability

To evaluate the system stability, the most common criteria used are the phase and gain margins that can indicate both absolute and relative stability. For the system considered here, one can compute the loop transfer function (LTF) as the relationship between input $u(k)$ and the output Y, as shown in Fig. 10. The corresponding state space representation is given by [35]

$$\begin{aligned} \begin{bmatrix} \hat{x}(k) \\ e(k) \end{bmatrix} &= \begin{bmatrix} \Phi - \Upsilon\Gamma L & K(k)C\Phi \\ \Upsilon\Gamma L & \Phi - K(k)C\Phi \end{bmatrix} \begin{bmatrix} \hat{x}(k-1) \\ e(k-1) \end{bmatrix} \\ &\quad + \begin{bmatrix} K(k)C\Gamma \\ (I - K(k)C)\Gamma \end{bmatrix} u(k-1) \end{aligned} \tag{36}$$

$$Y = \begin{bmatrix} L & 0 \end{bmatrix} \begin{bmatrix} \hat{x}(k) \\ e(k) \end{bmatrix} \tag{37}$$

where $\Upsilon = I - K(k)C$.

The transfer function of (36) can be obtained as

$$H_{LTF} = [L \quad 0][I - \phi z^{-1}]^{-1} \gamma z^{-1} \tag{38}$$

where ϕ, γ are the state transition and command matrices of (36). Given H_{LTF}, one can plot the Bode diagram and compute the gain and phase margin of the system in (36), as illustrated in next section. It is worthwhile to notice that this stability analysis applies when the system works close to the equilibrium since a linearized approximation of the Hunt–Crossley model around the equilibrium is used in the controller design.

Table 6
Stability analysis of the Hunt–Crossley model based force control system.

Model	Pole	G_m [dB]	φ_m [°]
HC	−2	29.2	64.3
	−5	29.0	63.0
	−8	28.8	61.7

Table 7
Transient responses of the three control force.

Rise time (s)			
Pole	HC	KB	Elastic
−2	1.21	1.11	1.28
−5	0.47	0.28	0.58
−8	0.23	0.08	0.36

5. Numerical studies

In this section, firstly stability of the Hunt–Crossley model based force control system as developed in last section is evaluated. The performance of the force controllers designed on the basis of different contact models are then compared.

5.1. Stability analysis for HC model based force control

Using the average values of the estimated parameters (see Table 2), the Hunt–Crossley contact model is given by the following equation

$$F_e(t) = 2 \cdot 10^3 x^{1.23}(t) + 4 \cdot 10^4 x^{1.23}(t)\dot{x}(t) \tag{39}$$

and the extra damping in (18) is set as $K_v = 0.05$.

For the AOB force control design, the linearized Hunt–Crossley equation in (11) is used. The discretization time is equal to T_s = 1 ms and the covariance matrices in (35) are selected as $Q_x = 10^{-6}$, $Q_p = 10^{-2}$, R = 0.005. The desired force input $r(k)$ (F_d) is defined as a step function of 5 N at 0.5 s with an initial value of 0.5 N to be consistent with the experimental setup in next section. Three different situations are studied with slower to faster rise time requirements, corresponding to closed loop system poles set at 2 rad/s, 5 rad/s and 8 rad/s respectively.

Gain (G_m) and phase (φ_m) margins greater than 10 dB and 30°, respectively, are usually required to guarantee good system robust-ness against external disturbances. Table 6 shows the results of the stability analysis for Hunt–Crossley model based force control sys-tem. In all three cases the system is stable and retains good gain and phase margins. It is also evident how faster poles decrease the system gain and phase margins.

5.2. Simulation comparison with linear model based control

The performance of the force controllers developed using AOB based on elastic and Kelvin–Boltzmann contact models are studied in this subsection. Nonlinear Hunt–Crossley model is used as the contact model in this simulation study to approximate the real tool-tissue interaction as justified in Section 3.

The values of the model parameters K, η and γ are set according to the estimated average values in Table 2, and the corresponding contact model equations are

$$\begin{aligned} F_{elastic}(t) &= 628.92x(t) \\ F_{KB}(t) &= 636.05x(t) + 156.92\dot{x}(t) - 0.052\dot{F}(t) \end{aligned} \tag{40}$$

In Fig. 11, the performance of all three force control systems, based on different contact models with different closed-loop poles, are illustrated for direct graphical comparison. The simulation results of the force control methods under study are summarized in Table 7.

Among the three developed force control methods, the one based on KB model shows the fastest rise time in all cases, but the downside is that when a fast pole is assigned overshoot appears in the exerted force as seen in Fig. 11(c), which should be minimized for surgical applications. In comparison, the HC model based control system shows slightly lower rise time and the elastic one presents the slowest response in all cases.

Remark 1. The elastic model represents the most often used contact model for force control in literature. The Kelvin–Boltzmann model is shown to be superior to elastic and other linear viscoelastic contact models in force control for soft tissues by the recent works [19]. Therefore, for the simulation studies of this section and the experimental studies in next section, only the elastic and Kelvin–Boltzmann model based controllers are considered for performance comparison with the Hunt–Crossley model based control method.

Remark 2. The performance of the linearized Hunt–Crossley model based controller may be affected by the neglected nonlinear terms, which are unknown and time-varying and thus are difficult to get a deterministic description. With the Kalman filter based AOB, the stochastically driven active state $p(k)$ aims to compensate the effect of neglected nonlinear terms in real time [34,35]. Simulation studies are carried out to test the range of validity of the controller based on linearized Hunt–Crossley model (around 5 N as an example) with AOB. It should be noted that for most MIS procedures the mean force applied during tissue grasps is around 5–11 N and even smaller for tissue suturing and other delicate operations [38,39]. So in this evaluation, the desired interaction force has been chosen as 2 N, 10 N, 15 N and 20 N with the system pole set to p = 5 rad/s (medium pole). The corresponding control performances are illustrated in Fig. 12, where it shows that for the controller based on a Hunt–Crossley model linearized around 5 N the force control performances are satisfactory with desired force command ranging from 2 to 15 N. When F_d = 20 N, a notable overshoot is observed (Fig. 12(f)) indicating that the control performance degrades when the system works too far away from the linearization point, which is a natural and understandable fact.

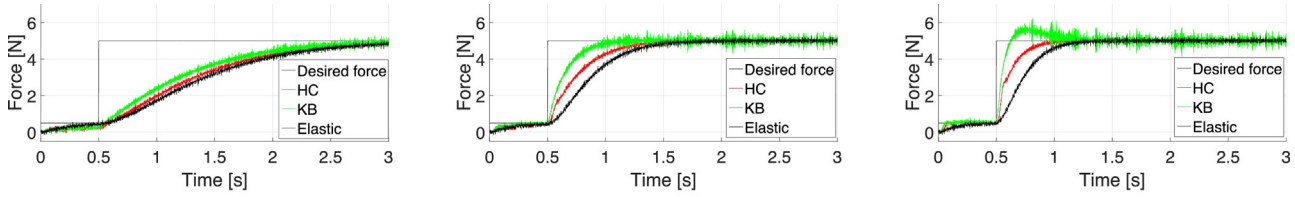

(a) $p = 2rad/s$ (b) $p = 5rad/s$ (c) $p = 8rad/s$

Fig. 11. System performances for different pole p assignments.

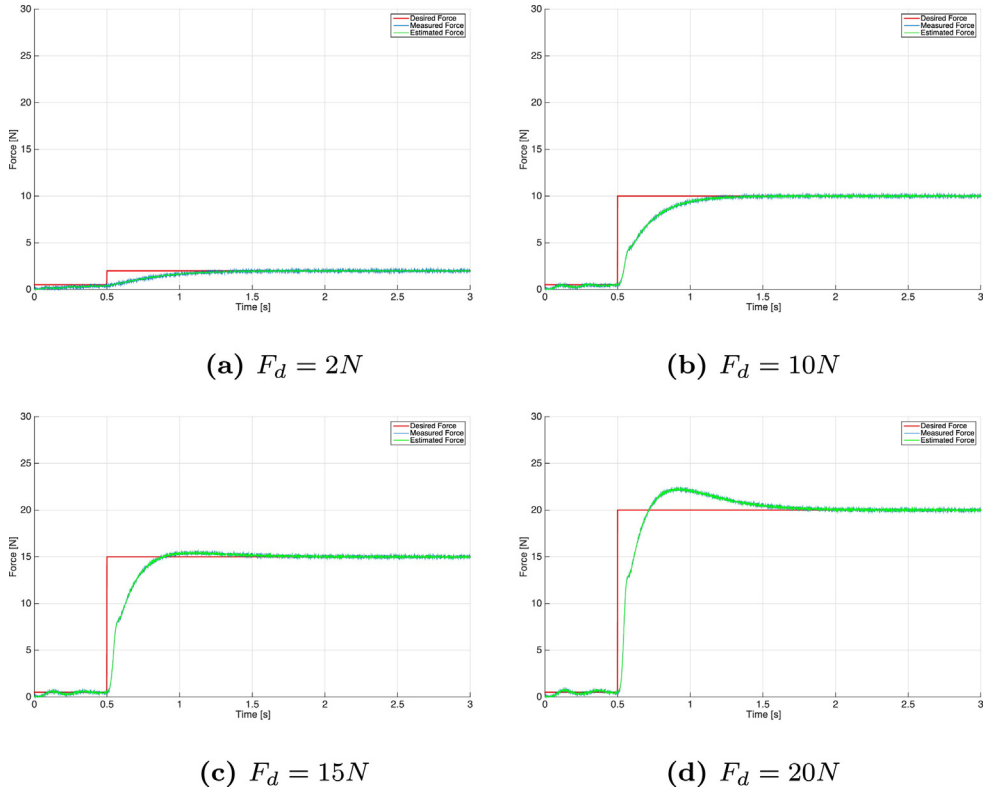

(a) $F_d = 2N$ (b) $F_d = 10N$

(c) $F_d = 15N$ (d) $F_d = 20N$

Fig. 12. Force control performances with different reference forces.

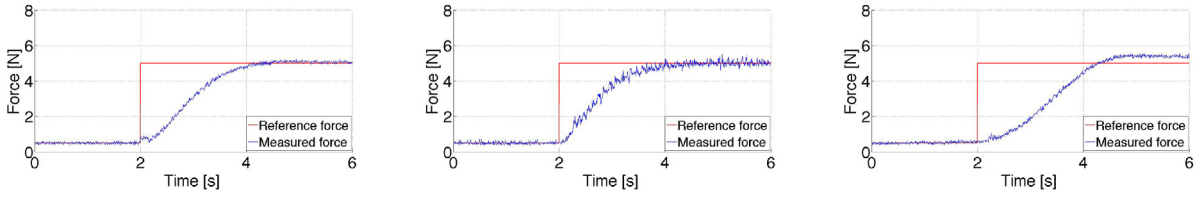

(a) $Hunt - Crossley$ (b) $Kelvin - Boltzmann$ (c) $Elastic$

Fig. 13. Experiment results with pole at $p = 2$ rad/s.

6. Experimental studies

In this section, the experimental results for the force control methods based on the linearized Hunt–Crossley, the elastic and the linear viscoelastic Kelvin–Boltzmann models are reported and compared.

6.1. System setup

The platform used for the experimental tests is the Raven-II robot system as introduced in Section 3 and illustrated in Fig. 4. A lamb's heart was used as the soft tissue sample for the experimental studies.

A step input of 5 N is set as the reference force command that should exert on a lamb's heart surface, in line with the simulation studies of last section. A small initial contact force around 0.5 N is exerted on tissue surface to ensure a real contact between robot and tissue at the beginning of experiment. Only motion along the normal direction (z axis) is allowed for the robot. The extra damping term K_v in the controller was set to $K_v = 0.05$, and based on the simulation studies the covariance matrices in AOB have been selected as follows

$$Q_{x(k)} = 10^{-6}, \quad Q_{p(k)} = 10^{-3}, \quad R(k) = 0.005$$

6.2. Experimental force control results

Figs. 13–15 show the performance of the control methods based on Elastic, KB, HC models and for different closed-loop poles ($p = 2$, 5, 8 rad/s) through *in vitro* experimental tests. To evaluate the control performance quantitatively, the contact force overshoot, rise time (RT) and the MFE/STD values of force tracking error (0–6 s) for each experiment are calculated and summarized in Table 8.

From the experimental results it can be observed that the elastic model based control always presents the slowest responses and Kelvin–Boltzmann model based control shows the smallest rising time. The Hunt–Crossley model based control shows slightly slower but comparable responses. Both Kelvin–Boltzmann and Hunt–Crossley model based control show similar force tracking performance in terms of MFE and STD, while the elastic model based control presents a bigger force tracking error.

Concerning overshoot, which is a criterion of particular importance for surgical applications, it can be noticed that elastic

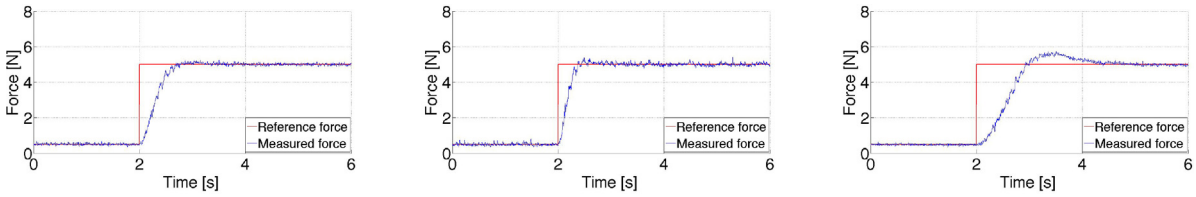

(a) $Hunt - Crossley$ (b) $Kelvin - Boltzmann$ (c) $Elastic$

Fig. 14. Experiment results with pole at $p = 5$ rad/s.

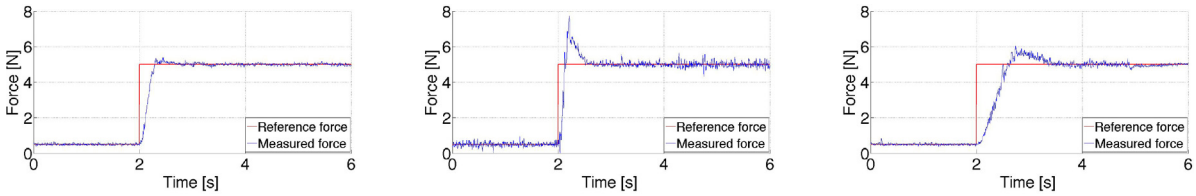

(a) $Hunt - Crossley$ (b) $Kelvin - Boltzmann$ (c) $Elastic$

Fig. 15. Experiment results with pole at $p = 8$ rad/s.

model based control shows overshoot even for the slow system pole $p = 2$ rad/s. The Kelvin–Boltzmann model based control remained stable for the fast pole $p = 8$ rad/s but the overshoot is over 50% (2.72 N) of the desired force (5 N). Comparatively, the Hunt–Crossley model based control showed very small overshoot for all three situations. In fact, for our experimental setup, the Hunt–Crossley model based control presented similar performance for even faster closed-loop poles, but Kelvin–Boltzmann model based control generated too big overshoot such that the Raven-II robot system entered "E-Stop" protection mode [36] for poles faster than $p = 8$ rad/s.

6.3. Discussion

Including the experiments introduced in detail in last subsection, the force control experiments have been conducted several times using different animal samples (beef muscle and lamb heart). The average control performance results for the experiments based on lamb heart are summarized in Table 9 and the ones based on beef muscle in Table 10. The averaged overall performance values of all experiments conducted are summarized in Table 11. From Tables 9–11, it is seen that all experiments lead to very similar conclusions of the control performances based on the three interaction models under comparison.

The elastic model based control shows the slowest responses, and overshoot is observed even for slow closed-loop poles. These are consistent with the recent work of [37] comparing the elastic model based and Kelvin–Boltzmann model based force control methods. The force control based on Kelvin–Boltzmann model always gives the fastest responses for different closed-loop poles but, as the downside, is prone to large overshoot especially for fast poles. This greatly limits its applicability for tasks with low overshoot requirements. The Hunt–Crossley model based control presents slightly slower responses, but always shows very small overshoots and therefore it is applicable to a wider range of force

Table 9
Average results for experiments using lamb heart.

Model	Pole	RT [s]	Overshoot [N]	MFE [N]	STD [N]
Elastic		1.49	0.69	0.89	1.70
KB	−2	1.05	0.46	0.56	1.14
HC		1.26	0.24	0.68	1.31
Elastic		0.52	0.73	0.32	1.19
KB	−5	0.20	0.51	0.11	0.66
HC		0.38	0.23	0.21	0.84
Elastic		0.32	0.94	0.19	0.94
KB	−8	0.05	2.19	0.002	0.55
HC		0.13	0.43	0.10	0.64

Table 10
Average results for experiments using beef muscle.

Model	Pole	RT [s]	Overshoot [N]	MFE [N]	STD [N]
Elastic		1.72	1.33	0.92	1.84
KB	−2	0.86	0.59	0.57	1.18
HC		1.30	0.64	0.68	1.40
Elastic		0.61	1.34	0.36	1.33
KB	−5	0.20	0.49	0.11	0.66
HC		0.41	0.49	0.21	0.86
Elastic		0.39	1.37	0.19	0.99
KB	−8	0.11	1.79	0.002	0.52
HC		0.20	0.78	0.10	0.65

Table 8
Experimental results.

Model	Pole	RT [s]	Overshoot [N]	MFE [N]	STD [N]
Elastic		1.71	0.81	0.86	1.59
KB	−2	1.02	0.67	0.57	1.14
HC		1.34	0.23	0.68	1.30
Elastic		0.62	0.72	0.33	1.14
KB	−5	0.22	0.40	0.11	0.62
HC		0.40	0.23	0.21	0.81
Elastic		0.35	1.02	0.19	0.91
KB	−8	0.09	2.72	0.002	0.58
HC		0.16	0.40	0.10	0.60

Table 11
Average results of all experiments.

Model	Pole	RT [s]	Overshoot [N]	MFE [N]	STD [N]
Elastic		1.60	0.95	0.87	1.76
KB	−2	0.97	0.51	0.55	1.16
HC		1.27	0.40	0.66	1.34
Elastic		0.55	0.98	0.32	1.24
KB	−5	0.20	0.50	0.11	0.66
HC		0.39	0.33	0.21	0.84
Elastic		0.34	1.11	0.19	0.96
KB	−8	0.08	2.03	0.002	0.54
HC		0.15	0.56	0.10	0.64

control tasks with requirements on both response time (efficiency) and overshoot (safety).

Experimental studies also reveal that the Kelvin–Boltzmann model based controller leads to chattering contact forces. This could be explained by the model Eq. (5), where the derivative of contact force is used whose measurement is usually very noisy.

A main limitation to our experimental study is that the hardware safety protection of Raven II system prevents us from further exploring the performance of each controller with harsher task requirements, e.g. to observe oscillation or even divergence in order to better evaluate the control system stability. This may be alleviated by carrying out the experimental study on a general purpose industrial robot. Also, so far the experiments were conducted based on *in vitro* tissue samples, *in vivo* animal tests will better evaluate different contact model based force control methods.

Both simulation and experimental studies confirm that the Hunt–Crossley model based force control system provides comparable response time and force control accuracy as Kelvin–Boltzmann model, but it presents smoother performance with much less overshoot than Elastic and KB model based control systems. This is particularly important for surgical applications, where overshoot should be minimized for safety reason and prompt response should be generated when a command is made. Therefore, the Hunt–Crossley model stands as the more suitable candidate to develop the force control scheme for robotic instrument and soft tissue interaction.

7. Conclusion

In the context of minimally invasive robotic surgery, the control of the interaction force between robotic instrument and soft tissue is an important research topic from both safety and efficiency point of view.

Most force control methods in literature, including some works for robotic tool-tissue force control, assume that the interaction between the robot and the operating environment can be estimated by a pure elastic model. To better describe the complex viscoelastic properties of soft tissue contact, more sophisticated models have been proposed. The Kelvin–Boltzmann model is one of the linear viscoelastic models that best describes these properties [19]. To improve modeling accuracy, the nonlinear properties of soft tissues must be considered as well, and it is necessary to explore nonlinear models like the Hunt–Crossley model, which has been reported as a more realistic option from the physical point of view.

In this work, Hunt–Crossley has been used for the first time in literature as the basis to design the interaction force controller. The design is based on state feedback regulation and active observer (AOB) techniques. Both simulation and *in vitro* experimental studies were carried out to evaluate the developed control method and compare its performance with other linear contact model based control methods. The Hunt–Crossley model based force controller is shown to be superior to other model based methods considering the main evaluation criteria in the scenario of robotic surgery such as response time, control accuracy and overshoot.

Acknowledgement

This work was supported by French Centre National de la Recherche Scientifique (CNRS) in collaboration with Politecnico di Milano, Italy.

References

[1] J.S. Park, G.S. Choi, K.H. Lim, Y.S. Jang, S.H. Jun, S052: a comparison of robot-assisted, laparoscopic, and open surgery in the treatment of rectal cancer, Surg. Endosc. 25 (1) (2011) 240–248.

[2] R.S. Poston, R. Tran, M. Collins, M. Reynolds, I. Connerney, B. Reicher, D. Zimrin, B.P. Griffith, S.T. Bartlett, Comparison of economic and patient outcomes with minimally invasive versus traditional off-pump coronary artery bypass grafting techniques, Ann. Surg. 248 (4) (2008) 638–646.

[3] G. Perigli, C. Cortesini, E. Qirici, D. Boni, F. Cianchi, Clinical benefits of minimally invasive techniques in thyroid surgery, World J. Surg. 32 (4) (2008) 45–50.

[4] M. Ghodoussi, S.E. Butner, Y. Wang, Robotic surgery: the transatlantic case, in: IEEE Int. Conf. on Robotics and Automation, vol. 21(3), 2002, pp. 1882–1888.

[5] M. Jacopec, S.J. Harris, F.R. Baena, P. Gomes, J. Cobb, B.L. Davies, The first clinical application of a "hands-on" robotic knee surgery system, J. Comput. Aided Surg. 6 (6) (2001) 329–339.

[6] R.H. Taylor, B.D. Mittelstadt, H.A. Paul, W. Hanson, P. Kazanzides, J.F. Zuhars, B. Williamson, B.L. Musits, E. Glassman, W.L. Bargar, An image-directed robotic system for precise orthopaedic surgery, IEEE Trans. Robot. Autom. 10 (3) (1994) 261–275.

[7] M.E. Allaf, S.V. Jackman, P.G. Schulam, J.A. Gadeddu, B.R. Lee, R.G. Moore, L.R. Kavoussi, Laparoscopic visual field. Voice vs foot pedal interfaces for control of the AESOP robot, Surg. Endosc. 12 (12) (1998) 1415–1418.

[8] S. Sastry, M. Cohn, F. Tendick, Millirobotics for remote, minimally invasive surgery, Robot. Auton. Syst. 21 (3) (1997) 305–316.

[9] F. Tendick, M.C.Çavuşoğlu, Human–machine interfaces for minimally invasive surgery, IEEE Eng. Med. Biol. Soc. 6 (1997) 2771–2776.

[10] M.R. Treat, A surgeon's perspective on the difficulties of laparoscopic surgery, in: Computer-integrated Surgery — Technology and Clinical Application, Cambridge, 1996, pp. 559–560.

[11] E. Dombre, G. Duchemin, P. Poignet, F. Pierrot, Dermarob: a safe robot for reconstructive surgery, IEEE Trans. Robot. 19 (5) (2003) 876–884.

[12] D. De Lorenzo, Y. Koseki, E. De Momi, K. Chinzei, A.M. Okamura, Coaxial needle insertion assistant with enhanced force feedback, IEEE Trans. Biomed. Eng. 60 (2) (2013) 379–389.

[13] N. Enayati, E. De Momi, G. Ferrigno, Haptics in robot-assisted surgery: challenges and benefits, IEEE Rev. Biomed. Eng. (2016) (in press).

[14] C.R. Wagner, N. Stylopoulos, P.G. Jackson, R. D-Howe, The benefit of force feedback in surgery: examination of blunt dissection, J. Presence: Teleoperators Virtual Environ. 16 (3) (2007) 252–262.

[15] W. Zarrad, P. Poignet, R. Cortesao, O. Company, Towards teleoperated needle insertion with haptic feedback controller, in: IEEE/RSJ Int. Conf. on Intelligent Robots and Systems, 2007, pp. 1254–1259.

[16] Y.C. Fung, Biomechanics: Mechanical Properties of Living Tissue, Springer, 1993.

[17] M. Machado, P. Moreira, P. Flores, H.M. Lankarani, Compliant contact force models in multi-body dynamics: evolution of the Hertz contact theory, Mech. Mach. Theory 52 (2012) 99–121.

[18] N. Diolati, C. Melchiorri, S. Stramigioli, Contact impedance estimation for robotic system, IEEE Trans. Robot. 21 (5) (2005) 925–935.

[19] P. Moreira, C. Liu, N. Zemiti, P. Poignet, Soft tissue force control using active observers and viscoelastic interaction model, in: IEEE Int. Conf. on Robotics and Automation, 2012, pp. 4660–4666.

[20] K.H. Hunt, F.R.E. Crossley, Coefficient of restitution interpreted as damping in vibroimpact, ASME J. Appl. Mech. 42 (52) (1975) 440–445.

[21] A. Haddadi, K. Hashtrudi-Zaad, Real-time identification of Hunt–Crossley dynamic models of contact environments, IEEE Trans. Robot. 28 (3) (2012) 555–566.

[22] S. Jeon, M. Harders, Haptic tumor augmentation: exploring multi-point interaction, IEEE Trans. Haptics 7 (4) (2014) 477–485.

[23] Y. Kobayashi, A. Kato, H. Watanabe, M.G. Fujie, Modeling of viscoelastic and nonlinear material properties of liver tissue using fractional calculations, J. Biomech. Sci. Eng. 7 (2) (2012) 177–187.

[24] L. Sciavicco, B. Siciliano, L. Villani, G. Oriolo, Robotics: Modeling, Planning and Control, Springer, 2009.

[25] E.J. Hunter, I.R. Titze, Refinements in modeling the passive properties of laryngeal soft tissue, J. Appl. Physiol. 103 (1) (2007) 206–219.

[26] D.W. Marhefka, D.E. Orin, Simulation of contact using a nonlinear damping model, in: IEEE Int. Conf. on Robotics and Automation, 1996, pp. 1662–1668.

[27] C. Liu, P. Moreira, N. Zemiti, P. Poignet, 3D force control for robotic-assisted beating heart surgery based on viscoelastic tissue model, in: IEEE Eng. in Medicine and Biology Soc., 2011, pp. 7054–7058.

[28] H. King, S.N. Kosari, B. Hannaford, Kinematic analysis of the Raven-II ™ research surgical robot platform. UWEE Technical Report, 2013.

[29] K. Levenberg, A method for the solution of certain nonlinear problems in least squares, Q. Appl. Math. 2 (1944) 164–168.

[30] D. Marquardt, An algorithm for least-squares estimation of nonlinear parameters, SIAM J. Appl. Math. 11 (2) (1963) 431–441.

[31] J. Park, O. Khatib, A haptic teleoperation approach based on contact force control, Int. J. Robot. Res. 25 (5–6) (2006) 575–591.

[32] K.J. Astrom, B. Wittenmark, Computer-controlled Systems: Theory and Design, Prentice Hall, 1997.

[33] F.L. Lewis, Applied Optimal Control and Estimation: Digital Design and Implementation, Prentice Hall, 1992.

[34] R. Cortesao, On Kalman active observers, J. Intell. Robot. Syst. 48 (2) (2007) 131–155.

[35] R. Cortesao, J. Park, O. Khatib, Real-time adaptive control for haptic telemanipulation with Kalman active observer, IEEE Trans. Robot. 22 (5) (2006) 987–999.

[36] M.J.H. Lum, D.C.W. Friedman, G. Sankaranarayanan, H. King, K. Fodero II, R. Leuschke, B. Hannaford, J. Rosen, M.N. Sinanan, The Raven: design and validation of a telesurgery system, Int. J. Robot. Res. 28 (9) (2009) 1183–1197.
[37] P. Moreira, N. Zemiti, C. Liu, P. Poignet, Viscoelastic model based force control for softtissue interaction and its application in physiological motion compensation, Comput. Methods Progr. Biomed. 116 (2) (2014) 52–67.
[38] J.D. Brown, J. Rosen, L. Chang, M.N. Sinanan, B. Hannaford, Quantifying surgeon grasping mechanics in laparoscopy using the blue DRAGON system, in: Medicine Meets Virtual Reality, vol. 98(12), 2004, pp. 34–36.
[39] A. Dubrowski, R. Sidhu, J. Park, H. Carnahan, Quantification of motion characteristics and forces applied to tissues during suturing, Am. J. Surg. 190 (1) (2005) 131–136.